Published in final edited form as:

J Phys Chem C Nanomater Interfaces. 2016 May 19; 120(19): 10530–10546. doi:10.1021/acs.jpcc.6b00875.

Size- and Shape-Controlled Synthesis and Properties of Magnetic-Plasmonic Core-Shell Nanoparticles

Elyahb Allie Kwizera[†,‡], **Elise Chaffin**[†,‡], **Xiao Shen**[ξ], **Jingyi Chen**[||], **Qiang Zou**[⊥], **Zhiming Wu**[⊥], **Zheng Gai**[⊥], **Saheel Bhana**[†], **Ryan O'Connor**[†], **Lijia Wang**[ξ], **Hitesh Adhikari**[ξ], **Sanjay R. Mishra**[ξ], **Yongmei Wang**[†,*], and **Xiaohua Huang**[†,*]

[†]Department of Chemistry, The University of Memphis, Memphis, TN 38152

[ξ]Department of Physics and Materials Science, The University of Memphis, Memphis, TN 38152

[||]Department of Chemistry, University of Arkansas, Fayetteville, AR 72071

[⊥]Center for Nanophase Materials Sciences, Oak Ridge National Laboratory, Oak Ridge, TN 37831

Abstract

Magnetic-plasmonic core-shell nanomaterials offer a wide range of applications across science, engineering and biomedical disciplines. However, the ability to synthesize and understand magnetic-plasmonic core-shell nanoparticles with tunable sizes and shapes remains very limited. This work reports experimental and computational studies on the synthesis and properties of iron oxide-gold core-shell nanoparticles of three different shapes (sphere, popcorn and star) with controllable sizes (70 to 250 nm). The nanoparticles were synthesized via a seed-mediated growth method in which newly formed gold atoms were added onto gold-seeded iron oxide octahedrons to form gold shell. The evolution of the shell into different shapes was found to occur after the coalescence of gold seeds, which was achieved by controlling the amount of additive (silver nitrate) and reducing agent (ascorbic acid) in the growth solution. First principles calculation, together with experimental results, elucidated the intimate roles of thermodynamic and kinetic parameters in the shape-controlled synthesis. Both discrete dipole approximation calculation and experimental results showed that the nanopopcorns and nanostars exhibited red-shifted plasmon resonance compared with the nanospheres, with the nanostars giving multispectral feature. This research has made a great step further in manipulating and understanding magnetic-plasmonic hybrid nanostructures and will make important impact in many different fields.

Graphical abstract

[*]Corresponding Author: Yongmei Wang, ; Email: ywang@memphis.edu. Phone: (901) 678 2629. Fax: (901) 678 3447. Xiaohua Huang, ; Email: xhuang4@memphis.edu. Phone: (901) 678 1728. Fax: (901) 678 3447

[‡]**Author Contributions**

These authors contributed equally.

Supporting Information. Supporting Information. Additional characterization of the synthesis of Au-seeded IO NPs and IO-Au core-shell NPs are available in supporting information. This information is available free of charge via the Internet at http://pubs.acs.org/.

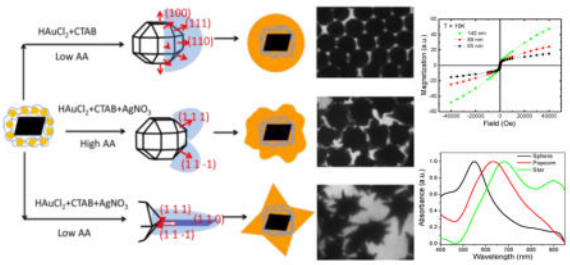

1. INTRODUCTION

Due to the combined magnetic and optical properties of their core and shell materials, magnetic-plasmonic core-shell nanoparticles (NPs) are useful in many areas including optical imaging,[1–3] magnetic resonance imaging,[2–8] biological separation,[9–17] molecular/cellular detection,[13–19] and cancer treatment,[3, 6–8, 11, 20–22] superior to solid magnetic and solid plasmonic NPs. For the existing magnetic-optical core-shell nanostructures, the core commonly consists of iron (Fe) or iron oxide (IO, Fe_3O_4 or γ-Fe_2O_3) and the shell is typically gold (Au) or silver (Ag). IO-Au core-shell NPs are particularly appealing because they have combined magnetic and optical properties of IO and Au NPs that can be individually tuned by changing the particle's size and shape,[23, 24] In addition, the Au shell is inert and allows for facile surface modification. During the past decade, a great deal of effort has been made on the synthesis of IO-Au core-shell NPs in the spherical shape.[25, 26] The synthetic methods can be organized into two major categories: (1) the reduction of an Au precursor in the presence of IO NPs with or without surface modifications [1, 27–30] and (2) the reduction of an Au precursor in the presence of Au-seeded IO NPs.[31–34] The second method is well received because the Au seed serves as the nucleation site to facilitate the growth of Au shell. However, current methods using Au-seeded IO NPs often use a multistep deposition of Au atoms in order to form a uniform Au shell. Generally, the IO-Au nanospheres (NSPs) exhibit localized surface plasmon resonance (LSPR) in the visible region, but large particles (> 150 nm) [32–34] or particles with a gap between the core and shell [1] show LSPR in the near infrared (NIR) region.

Anisotropic NPs offer greatly enhanced optical properties as compared with spherical counterparts due to their high curvature structure. For example, the peak E-field enhancement factor ($|E^2|/|E_0^2|$) of an Ag nanoprism is about 10 times higher than that of an Ag NSP.[35] This may lead to as much as 100 times stronger surface enhanced Raman scattering (SERS) signals for the nanoprisms as compared with the NSPs. Due to their strong SERS activities, Au-based NPs in popcorn and star shapes have been well used for SERS-based biomedical detections.[36–40] Anisotropic NPs could also offer new functions such as dynamic optical imaging because their optical properties are sensitive to the polarization of the light.[41] Additionally, anisotropic NPs allow for greater optical tunability than spherical ones. For example, the LSPR wavelength of Au nanorods (NRs) can be tuned from 620 to 960 nm by increasing the particle's aspect ratio from 2.4 to 5.7.[42] In contrast, the LSPR wavelength of Au NSPs can only shift from 520 to 570 nm when the size is increased from 9 to 99 nm.[43]

Despite the compelling anisotropy-associated properties and functions, the ability to synthesize and understand anisotropic IO-Au core-shell NPs remains very limited. In 2006, the Halas group synthesized IO-Au core-shell nanorices via a seed-mediated growth method.[44] The use of large rice-shaped IO NPs (longitudinal diameter over 300 nm) resulted in Au-coated IO NPs of the same shape. Later, the Wei group reported the synthesis of star-shaped IO-Au core-shell NPs.[41,45] In their method, IO-Au core-shell NSPs (9–16 nm) were firstly prepared in organic phase at high temperature by the reduction of Au^{3+} in the presence of small IO NPs (8–13 nm). These IO-Au core-shell NSPs were then used as seeds to form IO-Au core-shell NPs in a star shape. In our recent studies, we synthesized IO-Au core-shell NPs in pin [46] and oval shapes [17] using Ag-seeded IO nanospheres as the seeds. Although these anisotropic NPs are compact in size (less than 100 nm), they are polydisperse and often contaminated with large portion of spheres.

Here we report the facile synthesis of monodisperse IO-Au core-shell NPs of three different shapes: sphere, popcorn and star through a fine control of the thermodynamic and kinetic parameters of the seed-mediated growth method. We also demonstrate the tunability of the Au shell thickness for each shape, producing anisotropic NPs less than 100 nm. By combining experimental and computational approaches, we have gained a deeper understanding of the mechanism for the shape-controlled synthesis as well as the structure-property relationship of the resultant NPs. Not only have our studies made much progress in manipulating and understanding the magnetic-plasmonic core-shell nanosystem, but also provided a panel of high quality bifunctional nanostructures for biomedical detection and treatment.

2. EXPERIMENTAL AND THEORETICAL METHODS

2.1. Materials

All chemicals were purchased from Sigma-Aldrich unless specified.

2.2. Synthesis of IO NPs

Octahedral IO NPs were synthesized according to the method of Goon et al. [47] with modifications. In a typical procedure, 175 mg of iron sulfate ($FeSO_4$), 2.5 mL of 2.0 M potassium nitrate (KNO_3), 2.5 mL of 1.0 M sodium hydroxide (NaOH), and 5 mL of 8 mg/mL polyethyleneimine (PEI, branched, MW ~ 25,000) were added to 20 mL of nitrogen purged ultrapure water. Under the oxygen-free environment, the mixture was heated to 90°C under vigorous stirring, with continued heating at this degree for 2 h. During the heating process, the solution changed color from blue to black, indicating the formation of IO NPs. The NPs were purified by magnetic separation for 5 cycles and then redispersed in 20 mL of ultrapure water for further use.

2.3. Synthesis of Au-seeded IO NPs

Similar to the method by Goo et al,[47] we attached Au seeds to IO NPs to facilitate the growth of Au shell. Firstly, small Au NPs were synthesized by reduction of chloroauric acid ($HAuCl_4$, 25 mM) with sodium borohydride (0.2 M) in the presence of sodium citrate (0.85 mM). Then, they were attached to PEI-stabilized IO NPs via electrostatic interactions

(Scheme 1, step 1). In a typical procedure, 55 μL of 0.32 mg (Fe) PEI-stabilized IO NPs were added to 5 mL of as-prepared Au NPs and stirred for 45 min. After purification by three cycles of magnetic separation and washing, the solution was redispersed in 2.5 mL of 15 mg/mL PEI aqueous solution and heated at 60°C for 3 h. After purifications by three cycles of magnetic separation and washing, the Au-seeded IO NPs were redispersed in 1 mL of ultrapure water for further use.

2.4. Synthesis of IO-Au Core-shell Nanospheres (NSPs), Nanopopcorns (NPCs), and Nanostars (NSTs)

(Scheme 1, step 2). To make IO-Au core-shell NSPs, an Au growth solution was prepared by adding 200 μL of 10 mM $HAuCl_4$ into a 5 mL of 0.1 M cetyltrimethylammonium bromide (CTAB) aqueous solution. After mixing for 5 min, 32 μL of 100 mM ascorbic acid (AA) was added to reduce $HAuCl_4$ to $HAuCl_2$. Then, Au-seeded IO NPs with different amount from 100 to 800 μL was injected. The solution was stirred for 10 s followed by incubation for 2 h to allow complete growth of IO-Au core-shell NPs. To make NPCs, the same procedure was used except 30 μL of 10 mM silver nitrate ($AgNO_3$) and 90 μL of 100 mM AA were added into the growth solution. To make NSTs, the amount of $AgNO_3$ was the same as the NPCs, but the amount of AA was decreased to 32 μL, the same to NSPs.

2.5. Characterizations

All the as-prepared NPs were subjected to purification by magnetic separation before characterizations. The absorption spectra of all the NPs were collected using a VIS-NIR absorption spectrometer (Ocean Optics, Dunedin, FL). The magnetic properties of IO NPs were measured using a vibration sample magnetometer (Dexing Magnets, China) and those of IO-Au core-shell NPs via a quantum design superconducting quantum interference device (SQUID). Magnetic separation was performed with Qiagen 12-tube magnets. The size and morphology of the NPs were examined with a JEM1200EX II transmission electron microscope (TEM) (JEOL Ltd, Tokyo, Japan). Hydrodynamic size (HD) and zeta potential (ξ) were determined by dynamic light scattering (DLS) with a Particle Size Analyzer (Brookhaven Instruments Corp, NY, USA). Energy dispersive X-ray spectra (EDS) were taken on a Nova NanoSEM 640 (FEI, Hillsboro, Oregon). High resolution TEM (HRTEM) images were taken on an FEI Titan HRTEM (FEI, Hillsboro, Oregon).

2.6. First Principles Calculation

We use the Perdew–Burke–Ernzerhof (PBE) [48] version of the generalized-gradient approximation (GGA) exchange-correlation functional to calculate the adsorption energy of Ag on Au surfaces. We use projector-augmented-wave (PAW) potentials [49] and a plane-wave basis as implemented in the Vienna Ab-initio Simulation Package (VASP) code.[50] The kinetic energy cutoff of the plane wave basis is set to be 229.9 eV. The electronic self-consistent calculations are converged to 10^{-4} eV between two self-consistent steps. The structural relaxations are converged to 10^{-3} eV for the total energy difference between two ionic steps. All the adsorption energies are calculated for Ag coverage on the corresponding Au surfaces.

2.7. Discrete Dipole Approximation (DDA) Calculation

The IO-Au NSP, NPC, and NST extinction spectra were calculated using the widely-used DDA method as implemented by the DDSCAT 7.3 software.[51,52] The Au shells and IO (Fe_3O_4) cores were modeled using complex dielectric response functions of Johnson and Christy [53] and Goossens et al.[54], respectively. We developed a Fortran 90 code for the generation of the particle representations as material-specific point dipoles on a cubic lattice for the subsequent DDA calculations. The IO cores are represented as regular octahedrons with a specified edge length within an Au sphere of a specified diameter. Au conical tips are added to the surface of the spheres with additional dipoles added such that there are no gaps between the conical tips and the sphere surface. A sufficient number of dipoles ($>10^6$) were used in all calculations to achieve sufficient convergence of the calculated spectra.

3. RESULTS AND DISCUSSION

3.1. Synthesis and Properties of IO NPs

To make IO NPs, ferrous hydroxide ($Fe(OH)_2$) was firstly formed by precipitation of $FeSO_4$ in a basic solution and then oxidized to Fe_3O_4 with KNO_3 at 90°C in the presence of branched PEI in an oxygen-free environment. This method leads to aqueous soluble IO NPs with positive charges that allows for subsequent adsorption of negatively charged Au seeds. The DLS measurement showed a zeta potential around +34 mV, indicating the stabilization of the IO NPs by the positively charged PEI. TEM and SEM images showed that the IO particles had an octahedral shape, with average edge lengths of 35 nm (from ~ 100 NPs) (Figure 1A–C). The particles were well dispersed in water, giving an average HD of 52 nm (Figure 1D). HRTEM imaging revealed that the NPs were single crystals (Figure 1E). X-Ray diffraction analysis showed that they were composed of Fe_3O_4 (Figure 1F). EDS showed the characteristic Fe Kα1 peak at 6.4 keV (Figure 1G). The particles exhibited ferromagnetic properties, with a saturation magnetization M_s around 90 emu/g, a coercivity of 250 Oe and a retentivity of 20 emu/g (Figure 1H). A complete separation of the particles from the aqueous solution was observed within 5 min after the attachment of a Qiagen 12-tube magnet to the vials containing the particle solution (Figure 1H inset). This further confirmed the strong magnetic properties of the IO NPs.

3.2. Synthesis and Characterization of Au-seeded IO NPs

In order to form Au shell on the IO NPs, small Au NPs (< 10 nm) capped with citrate were adsorbed to the PEI-stabilized IO NPs to serve as the nucleation sites (see Scheme 1, Figure 2A). The negatively charged Au seed bound to the positively charged IO NPs via electrostatic interactions. Goon et al have shown that the amount of PEI on IO NPs is an important factor in determining the surface density of Au seed, with an increased amount of PEI leading to increased Au density.[47] We found that the stabilization of the Au-seeded IO NPs with additional PEI was also crucial to achieve high density Au seed. Without applying PEI after Au seed adsorption, the IO NPs were found to have a low surface density of the Au seed (Figure S1). In the presence of 5 mg/mL PEI, the surface density of the Au seed increased slightly. At 15 mg/mL PEI, the IO NPs were fully coated with Au NPs. A further increase of the PEI concentration resulted in a decrease in the Au seed density. These results demonstrate that sandwiching the Au seeds between two PEI layers is essential to achieve

Au-seeded IO NPs with high surface density. The Au-seeded IO NPs were averagely 55 nm by TEM and 78 nm by DLS (Figure 2B). They showed a LSPR at 523 nm due to the adsorbed Au seed (Figure 2C). HRTEM image showed that the Au seeds are single crystals enclosed by {111} facets (Figure 2D).

3.3. Synthesis of IO-Au Core-Shell NSPs

IO-Au core-shell NPs of different sizes and shapes were synthesized via a seed-mediated growth method. To form spherical particles, the Au-seeded IO NPs were injected into a growth solution containing $HAuCl_2$ (0.4 mM), CTAB (0.1 M), and AA (0.64 mM). $HAuCl_2$, CTAB and AA served as the Au precursor, capping agent, and reducing agent, respectively. $HAuCl_2$ was prepared in advance by the reduction of $HAuCl_4$ with AA. The reduction of Au^+ to Au^0 by AA is a surface catalyzed reaction. Thus, IO-Au core-shell NPs, rather than self-nucleated Au NPs, were preferentially formed in the presence of Au-seeded IO NPs. The appearance of a pink color indicates the growth of the Au-seeded IO NPs that completes within 1 h. Compared to the method by Goon et al,[47] this method only need a single step to form uniform Au shell from the Au-seeded IO NPs, avoiding cumbersome iterative depositions.

By adjusting the volume of the Au-seeded IO NP solution, IO-Au NPs of different sizes were synthesized. Figure 3 (A&B) show the TEM images and DLS data for the IO-Au NSPs prepared by injecting 800, 400, or 100 μL of the Au-seeded IO NP solution into a 5-mL growth solution. The particles were monodisperse, with average diameter (~ 100 NPs) of 77, 110 and 140 nm (Table 1). The HDs were 84, 122, and 155 nm, slightly larger than the sizes determined by TEM due to the coating and hydration layers. The thickness of Au shell is difficult to estimate because of the anisotropy of the octahedral IO core. When we considered the size along the diagonal direction of the IO core, we estimated that the average thickness of the Au shell for the three sizes of particles to be 14, 30 and 45 nm, respectively. Free IO NPs were not found in any samples, indicating complete conversion of the Au-seeded IO NPs to core-shell particles. In contrast, when the IO NPs were coated with low density Au seed, a significant amount of free IO NPs was found (Figure S2). The resultant particles were polydisperse, probably due to the formation of some solid Au NPs. The EDS spectra of all three sizes of particles revealed the presence of both Fe (Fe Kα1= 6.4 keV) and Au (Au Mα1 = 2.1 keV and Lα1 = 9.7 keV) (Figure 3C), which is in accord with the assumption of core-shell structures. Not surprisingly, the intensity of Au peaks increased and those of Fe peaks decreased with increasing Au shell thickness. When a magnetic field was applied, the particles were slowly isolated by the magnetic force, with a complete separation from the solution at 2.5 h for the 77 nm, 5 h for the 110 nm, and 8 h for the 140 nm NSPs (Figure 3D). This indicates that the synthesized NPs were indeed core-shell particles instead of solid Au NPs. We would like to point out that the elongated magnetic separation time does not indicate that the IO-Au core-shell NSPs have weak magnetic properties. This is because the separation time is not only proportional to the magnetic force on the NPs but also the mass of the NPs. The estimated mass of the 70, 110 and 140 nm IO-Au core-shell NSPs [is] 32, 130, and 278 times larger than IO NPs, respectivley. Thus, it is not suprising that it takes hours to separate the IO-Au core-shell NSPs from the solution due to the dramatic mass contribution from diamagnetic Au that has four times higher density than IO.

It is worth mentioning that further increasing the amount of Au-seeded IO NPs did not result in IO-Au core-shell NPs with thinner shells. When we added 1000 μL of Au-seeded IO NPs into the growth solution, we found the sample was composed of Au-seeded IO NPs but with larger seeds than the initially adsorbed Au seeds (Figure S3A). Unlike the initial Au-seeded NPs, these NPs are susceptible to aggregation during the drying process that is required for the sample preparation for TEM imaging. The NPs had a broad absorption spectrum with a strong LSPR at 541 nm (Figure S3B).These results indicate that the amount of Au precursor is insufficient for the formation of uniform core-shell structures with the injection of a high volume of Au-seeded IO NPs (> 800 μL).

3.4. Synthesis of IO-Au Core-Shell NPCs and NSTs

To synthesize anisotropic NPs, we added a small amount of $AgNO_3$ (60 μM final concentration) into the growth solution. A further control on the concentration of AA led to particles with different morphologies. The appearance of a blue color indicates the growth of the Au-seeded IO NPs that completes within 2 h. By increasing the concentration of AA by a factor of 2.5 (1.6 mM final concentration), IO-Au NPs with short and wide protrusions, which we referred to as popcorns, were produced (Figure 4A). Because the protrusions were heterogeneous, it was difficult to precisely quantify the size of the NPs. Thus, we have defined a base size in terms of the inner spherical IO-Au core (see illustration in Figure 4A inset). By adjusting the volume of Au-seeded IO NPs, IO-Au NPCs with different base sizes were synthesized. The injection of 800, 400, and 100 uL of Au-seeded IO NPs led to NPCs with an average base size of 65, 89, and 145 nm, respectively. The protrusions became larger when the particle's size increased, up to 65 nm in length and 62 nm in half widths for the 100 uL-sample (Table 1). DLS measurement indicated that these NPs were well dispersed in water, with the average HDs of 80, 110 and 170 nm for the three sized particles (Figure 4B). Similar to the IO-Au NSPs, we confirmed the core-shell structures of the NPCs through EDS measurements and magnetic separations. Figure 4C showed that both Fe and Au were detected by EDS. Because free IO NPs were not found in the TEM images, the Fe peaks shown in Figure 4C must be due the IO core in the IO-Au core-shell particles. The particles were completely separated from the aqueous solution by a 12-tube magnet at 5 h for the 65 and 89 nm particles and at 8 h for the 145 nm particles, which further confirmed their core-shell structures.

The IO-Au NSTs were synthesized using the same concentration of AA in the synthesis of the spheres. Figure 5A shows the TEM images of IO-Au NSTs prepared via the addition of 350, 250 or 100 μL of Au-seeded IO NP solutions. The average base sizes of these NPs were 70, 100, and 139 nm. Each particle had multiple tips of different lengths. The tips were markedly longer and thinner than the protrusions of the NPCs. For the small stars with a base size of 70 nm, the lengths of the tips ranged from 10 to 75 nm (Table 1). The lengths of the tips increased with the base size of the NPs. Tips as long as 145 nm were observed for the large stars. DLS characterization showed that the 70, 100 and 139nm NSTs had average HD of 105, 160 and 195 nm, respectively (Figure 5B). By tuning the Au shell thickness, we have made the IO-Au NSTs with an overall size smaller than 100 nm, which has not been achieved previously. Additionally, the IO cores in these NSTs have large size, ~ 4 times larger than those in previous studies.[45] Particles with larger IO core offer stronger magnetic

properties as the magnetic properties increase with the particle's size.[55] As for the IO-Au NSPs and NPCs, the EDS spectra of the NSTs showed the presence of both Fe and Au peaks for each sample, confirming the core-shell structure (Figure 5C). Magnetic separations were achieved using the Qiagen 12-tube magnets, leaving clear liquid solutions for all the three sizes of particles (Figure 5D). This further confirmed that the IO-Au NSTs were core-shell NPs rather than self-nucleated Au NPs.

Compared to the NSPs and NPCs, we found that the relative amount of Au precursor per particle, required to form uniform core-shell stars was significantly higher. Increasing the volume of Au-seeded IO NP solution to 500 μL or more failed to produce NSTs, but up to 800 μL of Au-seeded IO NP solution could be used to make core-shell spheres or popcorns. Figure S4 shows the TEM image and absorption spectrum of the particles prepared by injecting 600 μL of Au-seeded IO NPs into the growth solution. It is evident that the growth of Au shell was incomplete and more Au precursor was needed to complete the growth process. These particles had a LSPR peak around 630 nm and a shoulder peak around 910 nm, possibly resulting from assembled Au seeds on the IO NPs.

3.5. Mechanisms of the Shape-Controlled Synthesis

Previous studies on Si-Au core-shell NPs showed that the growth process begins with the growth of the adsorbed Au seeds into larger seeds followed by coalescence on the core surface, and finally, the formation of a continuous metallic shell.[56] This is believed to be the general growth process for the seed-mediated method in the preparation of metal nanoshells. For the formation of star-shaped Au shell, the studies by Wei and co-authors have implied that Au deposition at twined boundaries with net growth in the (111) direction is the dominate growth mechanism.[45] To further understand the mechanism of the shape-controlled synthesis using our system, we firstly followed the growth process of the core-shell NSPs, NPCs and NSTs with TEM imaging (Figure 6). We found that the NSPs grew at a much faster rate than either the NPCs or NSTs. At 5 min, the Au seeds already entered the coalescence step while no visible changes were observed for NPCs and NSTs. At 20 min, a continuous Au shell has formed for the NSPs while the NPCs and NSTs were still in the coalescence step. After 20 min, the NSPs continued to grow into larger particles and the NPCs and NSTs showed similar growth rates. The differences in the morphology of the particles were found at 30 min after seed injection. While the Au surface of the NPCs has become rough with short and wide protrusions, thin spikes have developed on the NSTs. This step occurred following the coalescence of the Au seeds. These spikes grew to form the sharp tip of the NSTs during subsequent growth. In the HRTEM images we found the typical (111) planes for Au on NSPs, the protrusions on NPCs and the tips on NSTs. A twin boundary was observed in the tip of NSTs, which was marked by the yellow line in the lower right image of Figure 6.

As described in the previous sections, the growth of the Au-seeded IO NPs into different geometries is controlled by adjusting the $AgNO_3$ and AA concentrations. Although the formation of core-shell NSPs does not require the presence $AgNO_3$, it is required for the formation of NPCs or NSTs. $AgNO_3$ has been widely used to assist in the preparation of Au nanorods and other anisotropic metal NPs.[57–59] It has also been used to form spiky Au

nanoshells from Ag-seeded polymer template. [60,61]. A proposed model to explain the role of Ag^+ in the synthesis of these anisotropic NPs is based on silver underpotential deposition (UPD), the reduction of Ag^+ to Ag^0 on a metal substrate with a surface potential less than the standard reduction potential.[62] Thus, Ag^+ ions are reduced and deposited onto the surfaces of Au seeds in the presence of reducing agent. This may explain the slower growth rate for Au NPCs and NSTs compared with the NSPs. To induce anisotropic growth, Ag deposition must occur at different rates on different crystal facets. To better understand the effects of Ag deposition for the particle growth, we calculated the adsorption energy of an Ag atom on Au (100), (110) and (111) surfaces using the first principles density functional theory method (Figure 7A-C). We found that the adsorption energy (the energy gain from adsorption) of Ag is highest on the (110) surface, with an energy gain of 3.0 eV/atom. This is followed by the (100) surface, where the adsorption energy is 2.7 eV. The adsorption energy of Ag is lowest on the (111) surface, which is 2.2 eV/atom. The results from first principles calculations are in agreement with previous empirical calculations of reduction potential of Ag^+ to Ag^0 using embedded atom method (EAM), which shows that the reduction potential of Ag^+ to Ag^0 is higher on (110) faces, followed by the (100) surface and (111) faces.[63, 64] Thus, Ag deposition is correspondingly faster on (110) facet, followed by (100) and (111) surfaces. With sufficient Ag^+ in the solution, Ag covers the (110) and (100) surfaces of Au seeds, blocking the adsorption of Au on these faces. This blocking effect leaves only the (111) surface for Au growth, which leads anisotropic growth of the Au.

To fully understand the anisotropic growth of Au into a specific shape, we first took a close look at the crystal structure of the tip of the Au NSTs. Figure 7D shows the proposed structure of the tip, which is composed by two of the {111} planes, marked as (1 1 1) and (1 1 −1). The tip extends towards the (1 1 0) direction. Figure 7E shows the HRTEM image of the tip, where the (1 1 1) and (1 1 −1) terminating planes are marked. According to our analysis, this image corresponds to a side view of the tip when it is observed along the (1 −1 0) direction. The insert of Figure 7E is an enlarged view of the lattice at the interior of the tip, showing the positions of each Au atom. Figure 7F shows the positions of atoms according to the proposed model in Figure 7D when they were viewed along the (1 −1 0) direction. It agrees well with the HRTEM image in Figure 7E, which confirms the proposed model in Figure 7D.

As mentioned above, when $AgNO_3$ is absent, the final form of the Au NP is spherical. This is because all the {100}, {110}, and {111} surfaces on an Au seed are available for Au deposition, as shown in Figure 7G, leading to a nearly isotropic growth of the Au shell. On the other hand, when $AgNO_3$ is present, Ag will block the {110} and {100} surfaces of the Au seed, leaving the {111} surfaces for Au deposition. The growth of the NPs into popcorns or stars is a kinetic control on the Au deposition. This is achieved by controlling the concentration of AA that controls the reduction rate of Au^+ to Au^0. As shown in Figure 7H, when the reduction of Au^+ is fast, the Au deposition happens at the entire (111) facet, leading to the growth of Au island along the (111) direction. Such mechanism is confirmed by the HRTEM image of the tip of the NPC, which shows that the tip of NPC grows along the {111} direction. As illustrated in Figure 7H, the growth of tip can happen along different {111} directions, such as (1 1 1) and (1 1 −1), which lead to a popcorn structure for the IO-Au core-shell NPs. On the other hand, when the reduction of Au^+ to Au^0 is slow, the

deposition of Au happens mainly at the ridge formed by two {111} planes, for example the (1 1 1) and (1 1 −1) planes in Figure 7I. This is because the Au atoms at the ridge are more under coordinated than the atoms at the center of the facet, which makes them bind the adsorbed Au atoms more strongly. Also, the electrical field is stronger at the ridge than at the center of the facet due to the larger curvature at the ridge, making the reduction of Au^{+} faster at the ridge. The growth of Au on the ridge can be viewed as cohesive growth along two {111} direction, as shown in Figure 7I. Such cohesive growth from two planes can lead to the formation of a twin boundary along the (110) direction, shown as the dark blue plane in Figure 7I and the yellow line in the HRTEM in the lower right panel of Figure 6.

3.6. Magnetic Properties of IO-Au Core-shell NSPs, NPCs and NSTs

From the aforementioned magnetic separation experiments, it can be seen that the IO-Au core-shell NPs preserved the magnetic properties of the core. We additionally examined the temperature dependence of the magnetization of IO-Au core-shell NSPs, NPCs and NSTs. The results showed that all these NPs (around 100 nm in the base size) had almost identical temperature dependence (Figure 8A). At room temperature (300 K), they exhibited similar ferromagnetic properties (Figure 8B) as the ferromagnetic IO core, which were indicated by the hysteresis loops under low field (Figure 8B inset). At low temperatures (10 K), the field dependence of the magnetization of the particles showed both the ferromagnetic and paramagnetic contributions (Figure 8C), consisting with the dramatic increase of the temperature dependence of the magnetization at low temperature. Since the IO core was ferromagnetic, the paramagnetic responses might originate from the Au shell. To further demonstrate the paramagnetic behavior of the Au shell, we measured the M-T and M-H curves of IO-Au NPs of three sizes of particles using the NPCs as a model system (Figure 8D–F). The results showed that the Au shell does not affect the ferromagnetic behavior at 300 K. However, the IO-Au NPs with thicker Au shell showed higher paramagnetic contribution than those with thinner shell at 10 K. The hysteresis loops at 10 K (insets in Figure 8C&F) are larger than those at 300 K (insets in Figure 8B&E) due to their higher retentivity at low temperature.

It is well known that Au is a diamagnetic material in the bulk state. At the nanoscale, positive magnetization has been reported in particles smaller than 5 nm.[65] For the magnetic-plasmonic core-shell nanostructure system, it has been widely studied and observed that the NPs exhibit the same magnetic (superparamagnetic or ferromagnetic) behavior as the core at room temperature,[1, 6, 9, 12, 17, 20, 32, 46, 66–68] similar to what we have observed in our particles. At low temperature, several studies have shown that the NPs follow the ferromagnetic properties of the core.[69–74] In our studies, however, we have observed the paramagnetic properties of the IO-Au core-shell nanosystem at low temperature. It has been recognized that the magnetic material could spin polarize the Au conduction electrons at the IO-Au interface and thus result in magnetization of the surrounding nonmagnetic Au.[75] However, this does not provide an explanation for the increased paramagnetic properties with increasing Au shell thickness. We therefore believe that the external Au surface plays an important role. Research has shown that charge transfer between a thiol ligand and Au surface exists and are ascribed as a major reason for the observed ferromagnetic properties of thiolated Au NPs.[76] In our system, CTAB is the capping agent. It has been suggested that

CTAB binds to Au via Br^- and is counterbalanced by CTA^+ in a bilayer structure.[77–79] This suggests that charge transfer between Br^- and Au may occur, which would enhance the electron mobility and thus the surface induced magnetism of Au.

Addition of Au shell onto IO NPs generally leads to a dramatic reduction of the amplitude of the magnetization of IO NPs due to the mass contribution of the diamagnetic Au that has 4 times higher density than Au. For example, in the studies by Halas and co-workers,[33] coating tetracubic IO NPs with 10.9 nm Au shell decreased M_s from 15 emu/g to 0.5 emu/g. To examine the effect of Au coating on the amplitude of the magnetization of IO NPs in our IO-Au core-shell system, we used the 145 nm IO-Au core-shell NPCs as the model and quantitatively measured the M-H curve at 300 K (Figure S5). The M_s of the IO-Au core-shell NPCs is 0. 20 emu/g. To explain whether Au coating had adverse effect, we estimated the theoretical M_s of the 145 nm IO-Au core-shell NPs based on the M_s of IO NPs, densities of IO and Au and the dimension of the core-shell NPCs (Table 1). We took an assumption that each popcorn is composed of 6 protrusions, with each protrusion modeled as a conical Au tip with length of 20 nm and width of 30 nm. Based on these parameters, the calculated M_s of the IO-Au core-shell NPCs is 0.28 emu/g, which is comparable to the experimental value. It is also worth to mention that we did not take into account of the mass contribution from the diamagnetic PEI that was coated onto Au-seeded IO NPs before the growth of Au shell and the CTAB capping molecules on the Au surface. Further, some popcorns have more than 6 protrusions and have larger protrusions. These additional factors will further reduce the theoretical M_s value. Thus, the addition of Au shell did not play significant adverse effect on the magnetic properties of the IO core. The reduction of the magnetization after Au coating is mainly due to the dramatic increase of the mass of the core-shell NPs (> 300 times for the 145 nm IO-Au core-shell NPCs compared to the IO NPs) by the Au shell.

3.7. Optical Properties of IO-Au Core-shell NSPs, NPCs and NSTs

The IO-Au NSPs exhibited LSPR bands in the visible region from 530 to 600 nm depending on the size of the particles (Figure 9A). Increasing the size from 77 to 140 nm by increasing Au shell thickness led to a red shift of the LSPR from 538 to 575 nm. In our previous computational study using extended Mie theory, we found a blue shift of the LSPR when the thickness of Au shell was increased from 2 to 17.5 nm, but a red shift with further increase of Au shell thickness on a 15 nm diameter IO core.[80] In this study, the shell thicknesses were more than 14 nm and, thus, it was not surprising that we observed red shifted LSPR for particles with increased Au shell thicknesses. The absorption coefficients of these NPs have yet to be determined. However, it is worthy to note that the absorption spectra were obtained from the as-prepared particle solutions. Thus, the particle concentration depends on the amount of Au-seeded NPs injected into the growth solution. Assuming that all the Au-seeded NPs were converted to core-shell particles, we estimated from the measured LSPR intensities that the absorption coefficients of the 110 and 140 nm IO-Au NSPs are 2.5 and 9 times higher than that of the 77 nm IO-Au NSPs due to the increase on the size of the particles.

The measured UV-Vis spectra of the NPCs are shown in Figure 9B. The spectra shows a LSPR peak at 600, 633 and 665 nm for the NPCs with base sizes of 65, 89 and 145 nm,

respectively. Note that the overall sizes of the particles are slightly larger due to the protrusions on the surface of Au. Similar to the NSPs, an increase in the Au shell thickness led to red shifted LSPR bands. Compared to the NSPs of similar size, the LSPR peaks of the NPCs were shifted to longer wavelengths and the bands were broadened, owing to the anisotropic Au shell of the NPCs. Different from the NSPs and NPCs, the NSTs show three distinct peaks around 550 nm (weak), 700 nm (strong) and over 850 nm (strong) (Figure 9C). While the plasmon resonance in the visible region is insensitive to the particle size, it red shifts for the two peaks in the NIR region when the size is increased. When the base size of the particles was increased from 70 to 100 and 139 nm, the plasmon resonance for the middle peak was shifted from 660 to 684 and 715 nm. The plasmon resonance for the red-most peak was shifted to 920 nm and to a position over 950 nm that is out of the detection range of our spectrometer. It is also realized that the NSTs exhibit most red-shifted plasmon resonance compared to the NSPs and NPCs due to the elongated tip structure of the stars. Taking into account of the differences in the concentrations of NPs used in the absorption measurements, we have estimated that the ratio of the absorption coefficients of the 65, 89 and 145 nm NPCs is roughly 1: 1.6: 8.3 and that of 70, 100 and 139 nm NSTs is 1: 1.4: 2.8. Due to the anisotropic structures, both IO-Au NPCs and NSTs have great potential for SERS-based applications. The SERS activities also largely depend on the excitation laser wavelength. Due to their differences in the optical properties, the NPCs are expected to give strong SERS signals at 632 nm excitation while the NSTs are expected to give strong SERS signals at 785 nm.

To gain better understanding on the effects of size and morphology on the optical properties of IO-Au core-shell NPs, we have used the DDA method to calculate the extinction spectra of IO-Au core-shell NPs of spheres, popcorns and stars with varied shell thickness considering the particle's dimension given by TEM. Figure 10A shows the calculated extinction spectra for three sizes of IO-Au NSPs with octahedral cores (edge length a = 35 nm). With increasing sizes from 70 nm to 100 nm and 140 nm (due to increasing Au shell thickness), the peak width broadens and the peak maximum red shifts from 563 to 576 and 626 nm. The observed trends for the calculated spectra match favorably with the experimental results shown in Figure 9A.

For the NPCs and NSTs, we have chosen to investigate the effects of adding tips to the three sizes of NSPs on their respective extinction spectra as it is difficult to represent the synthesized popcorn or star samples in a single particle calculation. Six conical tips with lengths (L) of 20 nm for NPCs and 40 nm for NSTs were added to the surfaces of the IO-Au NSPs along the x, y, and z axis. The width (w) of the tips for both NPCs and NSTs is 30 nm. Figure 10B and 10C shows the calculated extinction spectra for NPCs and NSTs with the base sizes of 70 nm, 100 nm and 140 nm. The results show that the addition of tips results in extinction spectra with multiple LSPR peaks. When the tip is short (the popcorn), the multiple peaks are not well resolved, resulting in a spectrum consisting of a broad peak. Comparing to the IO-Au NSPs shown in Figure 10A, the predominant LSPR peak for the NPCs is red shifted to over 600 nm (630, 632, and 657 nm respectively). The original peak in the NSP spectrum appears as a shoulder around 550 nm. These spectra agree reasonably with experimental spectra shown in Figure 9B. Increasing the length of the tips to 40 nm (the star) results in the appearance of additional LSPR peaks. As we can see in Figure 10C,

the NSTs are characterized by two distinct peaks at 740 and 870 nm and two weaker peaks around 550 and 640 nm. Previous computational studies by Hao et al. using the finite-difference time-domain (FDTD) method showed similar spectral features for solid Au NSTs.[81] They explained that the multiple plasmon resonances result from the hybridization of the core and tip plasmons. We speculate that the peaks shown in Figure 10C are likely a similar result from the hybridization of plasmons associated with the IO-Au spherical core and the Au tips. The first peak around 550 nm could be mainly due to the plasmon resonance of the IO-Au NSP core but with a finite contribution from the tip plasmons. The peaks corresponding to additional LSPR modes at 640, 740, and 870 nm are likely the result of plasmonic coupling of the core and tips.

By increasing the base sphere size of the NSTs without changing the tip dimensions, we observe an increase in the intensities of the first two LSPR peaks within 700 nm, but a reduction in intensities of the peaks at longer wavelength (~740 and ~870 nm), with only small shifts of the peak positions. This feature is also observed in experimental spectra for NSTs shown in Figure 10C. The correlation between the DDA calculated and the experimental NST spectra is not as strong as for the NSP and NPC spectra. This is not surprising as the experimental spectra have been collected from a bulk sample of IO-Au NSTs with varied number and length of tips while the calculated spectra from a single particle with fixed number and length of the tips. We envision that the number and length of the Au tips will be the major players in further tuning the optical properties of the IO-Au NSTs. The exact correlation between observed LSPR peaks and the NST properties of tip length, tip width and number of tips will be investigated in detail in a future study.

4. CONCLUSIONS

In conclusion, we have synthesized monodisperse IO-Au core-shell NPs in sphere, popcorn and star shapes with tunable Au shell thickness, leading to compact magnetic-plasmonic NPs less than 100 nm in each shape. We have shown that the shape was evolved after coalescence of Au seeds on the IO core. Deposition of silver atoms onto Au surface led to anisotropic NPs due to the difference in the adsorption energy of Ag on different Au lattice planes. The growth of the NPs into popcorns or stars is a kinetic control on the deposition of newly formed Au atoms through controlling the reduction speed of Au precursors. This provides microscopic insights into the engineering of advanced plasmonic-based nanomaterials. The IO-Au core-shell NPs exhibit strong magnetic properties and tunable optical properties depending on the shape. The IO-Au NPCs and NSTs showed red-shifted localized surface plasmon resonance compared with the NSPs, with the nanostars giving strong plasmon resonance in the near infrared region. The NSTs showed distinct multiple LSPR modes due to the elongated tip structure on the IO-Au spherical core. These highly integrated bifunctional nanostructures will have significant applications for biomedical and materials research.

Supplementary Material

Refer to Web version on PubMed Central for supplementary material.

Acknowledgments

Funding Sources

The work is supported by National Institutes of Health (Grant No. 1R15 CA 195509-01).

We gratefully acknowledge the support from the National Institutes of Health (Grant No. 1R15 CA 195509-01).

References

1. Jin Y, Jia C, Huang SW, O'Donnel M, Gao X. Multifuncional Nanoparticles as Coupled Contrast Agents. Nat Commun. 2010; 1:1–8. [PubMed: 20975674]
2. Cai H, Li K, Shen M, Wen S, Luo Y, Peng C, Zhang G, Shi X. Facile Assembly of Fe_3O_4@Au Nanocomposite Particles for Dual Mode Magnetic Resonance And Computed Tomography Imaging Applications. J Mater Chem. 2012; 22:15110–15120.
3. Larson TA, Bankson J, Aaron J, Sokolov K. Hybrid Plasmonic Magnetic Nanoparticles As Molecular Specific Agents For MRI/Optical Imaging And Photothermal Therapy Of Cancer Cells. Nanotechnol. 2007; 18:325101/1–8.
4. Cho SJ, Jarrett BR, Louie AY, Kauzlarich SM. Gold-coated Iron Nanoparticles: A Novel Magnetic Resonance Agent For T1 And T2 Weighted Imaging. Nanotechnol. 2006; 17:640–644.
5. Kumagai M, Sarma TK, Cabral H, Kaida S, Sekino M, Herlambang N, Osada K, Kano MR, Nishiyama N, Kataoka K. Enhanced In Vivo Magnetic Resonance Imaging of Tumors by Pegylated Iron-Oxide–Gold Core–Shell Nanoparticles with Prolonged Blood Circulation Properties. Macromol. 2010; 31:1521–1528.
6. Ji X, Shao R, Elliott AM, Stafford RJ, Esparza-Coss E, Bankson JA, Liang G, Luo ZP, Park K, Markert JT, et al. Bifunctional Gold Nanoshells with a Superparamagnetic Iron Oxide-Silica Core Suitable for both MR Imaging And Photothermal Therapy. J Phys Chem C. 2007; 111:6245–6251.
7. Melancon MP, Elliott A, Ji X, Shetty A, Yang Z, Tian M, Taylor B, Stafford RJ, Li C. Theranostics With Multifunctional Magnetic Gold Nanoshells: Photothermal Therapy And T2* Magnetic Resonance Imaging. Invest Radiol. 2011; 46(2):132–140. [PubMed: 21150791]
8. Li J, Hu Y, Yang J, Wei P, Sun W, Shen M, Zhang G, Shi X. Hyaluronic Acid- Modified Fe_3O_4@Au Core/Shell Nanostars for Multimodal Imaging and Photothermal Therapy of Tumors. Biomaterials. 2015; 38:10–21. [PubMed: 25457979]
9. Wu CH, Huang YY, Chen P, Hoshino K, Liu H, Frenkel EP, Zhang JXJ, Sokolov KV. Versatile Immunomagnetic Nanocarrier Platform for Capturing Cancer Cells. ACS Nano. 2013; 7:8816–8823. [PubMed: 24016305]
10. Park HY, Schadt MJ, Wang L, Lim IS, Njoki PN, Kim SH, Jang MY, Luo J, Zhong CJ. Fabrication of Magnetic Core@Shell Fe Oxide@Au Nanoparticles for Interfacial Bioactivity and Bio-separation. Langmuir. 2007; 23:9050–9056. [PubMed: 17629315]
11. Fan Z, Shelton M, Singh AK, Senapati D, Khan SA, Ray PC. Multifunctional Plasmonic Shell–Magnetic Core Nanoparticles For Targeted Diagnostics, Isolation, And Photothermal Destruction Of Tumor Cells. ACS Nano. 2012; 6:1065–1073. [PubMed: 22276857]
12. Pham TTH, Cao C, Sim SJ. Application of Citrate-Stabilized Gold-Coated Ferric Oxide Composite Nanoparticles for Biological Separations. J Magn Magn Mater. 2008; 320:2049–2055.
13. Bao F, Yao JL, Gu RA. Synthesis Of Magnetic Fe_2O_3/Au Core/Shell Nanoparticles For Bioseparation And Immunoassay Based On Surface-Enhanced Raman Spectroscopy. Langmuir. 2009; 25:10782–10787. [PubMed: 19552373]
14. Tamer U, Gündoğdu Y, Boyacl IH, Pekmez K. Synthesis of Magnetic Core–Shell Fe_3O_4–Au Nanoparticle for Biomolecule Immobilization and Detection. J Nanopart Res. 2010; 12:1187–1196.
15. Lin L, Crew E, Yan H, Shan S, Skeete Z, Mott D, Krentsel T, Yin J, Chernova NA, Luo J, et al. Bifunctional Nanoparticles for SERS Monitoring And Magnetic Intervention of Assembly And Enzyme Cutting of DNAs. J Mater Chem B. 2013; 1:4320–4330.

16. Zhang L, Xua J, Mi L, Gong H, Jiang S, Yu Q. Multifunctional Magnetic–Plasmonic Nanoparticles For Fast Concentration And Sensitive Detection Of Bacteria Using SERS. Biosens Bioelectron. 2012; 31:130–136. [PubMed: 22036668]
17. Bhana S, Chaffin E, Wang Y, Mishra SR, Huang X. Capture and Detection Of Cancer Cells in Whole Blood With Magnetic-Optical Nanoovals. Nanomedicine(Lond). 2014; 9:593–606. [PubMed: 23763633]
18. Zhou X, Xu W, Wang Y, Kuang Q, Shi Y, Zhong L, Zhang Q. Fabrication Of Cluster/Shell Fe3O4/Au Nanoparticles And Application In Protein Detection via a SERS Method. J Phys Chem C. 2010; 114:19607–19623.
19. Liang CH, Wang CC, Lin YC, Chen CH, Wong CH, Wu CY. Iron oxide/gold Core/shell Nanoparticles For Ultrasensitive Detection Of Carbohydrate Protein Interactions. Analy Chem. 2009; 81:7750–7756.
20. Kayal S, Ramanujan RV. Anti-cancer Drug Loaded Iron–Gold Core–Shell Nanoparticles (Fe@Au) For Magnetic Drug Targeting. J Nanosci Nanotechnol. 2010; 10:1–13.
21. Chung RJ, Shih HT. Preparation of Multifunctional Fe@Au Core-Shell Nanoparticles with Surface Grafting as a Potential Treatment for Magnetic Hyperthermia. Materials. 2014; 7:653–661.
22. Guo Y, Zhang Z, Kim DH, Li W, Nicolai J, Procissi D, Huan Y, Han G, Omary RA, Larson AC. Photothermal Ablation of Pancreatic Cancer Cells with Hybrid Iron-Oxide Core Gold-Shell Nanoparticles. Int J Nanomed. 2013; 8:3437–3446.
23. de Montferrand C, Hu L, Milosevic I, Russier V, Bonnin D, Motte L, Brioude A, Lalatonne Y. Iron Oxide Nanoparticles with Sizes, Shapes and Compositions Resulting In Different Magnetization Signatures as Potential Labels For Multiparametric Detection. Acta Biomater. 2013; 9:6150–6157. [PubMed: 23207434]
24. Jain PK, Lee KS, El-Sayed IH, El-Sayed MA. Calculated Absorption and Scattering Properties of Gold Nanoparticles Of Different Size, Shape, And Composition: Applications in Biological Imaging and Biomedicine. J Phys Chem B. 2006; 110:7238–7248. [PubMed: 16599493]
25. Salihov SV, Ivanenkov YA, Krechetov SP, Veselov MA, Sviridenkova NV, Savchenko AG, Klyachko NL, Golovin YI, Chufarova NV, Beloglazkina EK, et al. Recent Advances in the Synthesis of Fe_3O_4@Au core/shell Nanoparticles. J Magn Magn Mater. 2015; 394:173–178.
26. Wang L, Park HY, Lim SI, Schadt MJ, Mott D, Luo J, Wang X, Zhong CJ. Core@shell Nanomaterials: Gold-Coated Magnetic Oxide Nanoparticles. J Mater Chem. 2008; 18:2629–2635.
27. Lyon JL, Fleming DA, Stone MB, Schiffer P, Williams ME. Synthesis of Fe Oxide Core/Au Shell Nanoparticles by Iterative Hydroxylamine Seeding. Nano Lett. 2004; 4(4):719–723.
28. Wang L, Luo J, Maye MM, Fan Q, Rendeng Q, Engelhard MH, Wang C, Lin Y, Zhong CJ. Iron Oxide–gold Core–shell Nanoparticles and Thin Film Assembly. J Mater Chem. 2005; 15:1821–1832.
29. Xu Z, Hou Y, Sun S. Magnetic Core/Shell Fe_3O_4/Au and Fe_3O_4/Au/Ag Nanoparticles with Tunable Plasmonic Properties. J Am Chem Soc. 2007; 129(28):8698–8699. [PubMed: 17590000]
30. Wheeler DA, Adams SA, López-Luke T, Torres-Castro A, Zhang JZ. Magnetic Fe_3O_4-Au Core-shell Nanostructures for Surface Enhanced Raman Scattering. Ann Phys (Berlin). 2012; 524:670–679.
31. Chin SF, Iyer KS, Raston CL. Facile and Green Approach to Fabricate Gold and Silver Coated Superparamagnetic Nanoparticles. Cryst Growth Des. 2009; 9:2685–2689.
32. Wang L, Bai J, Li Y, Huang Y. Multifunctional Nanoparticles Displaying Magnetization and Near-IR Absorption. Angew Chem Int Ed. 2008; 47:2439–2442.
33. Levin CS, Hofmann C, Ali TA, Kelly AT, Morosan E, Nordlander P, Whitmire KH, Halas NJ. Magnetic-plasmonic Core-shell Nanoparticles. ACS Nano. 2009; 3:1379–1388. [PubMed: 19441794]
34. Zhang Q, Ge J, Goebl J, Hu Y, Sun Y, Yin Y. Tailored Synthesis of Superparamagnetic Gold Nanoshells with Tunable Optical Properties. Adv Mater. 2010; 22:1905–1909. [PubMed: 20526992]
35. Hao E, Schatz G, Hupp J. Synthesis and Optical Properties of Anisotropic Metal Nanoparticles. J Fluor. 2004; 14:331–341.

36. Lu W, Singh AK, Khan SA, Senapati D, Yu H, Ray PC. Gold Nano-Popcorn-Based Targeted Diagnosis, Nanotherapy Treatment, and In Situ Monitoring of Photothermal Therapy Response of Prostate Cancer Cells Using Surface-Enhanced Raman Spectroscopy. J Am Chem Soc. 2010; 132:18103–18114. [PubMed: 21128627]
37. Fan Z, Senapati D, Khan SA, Singh AK, Hamme A, Yust B, Sardar D, Ray PC. Popcorn-Shaped Magnetic Core-Plasmonic Shell Multifunctional Nanoparticles for the Targeted Magnetic Separation and Enrichment, Label-Free SERS Imaging, and Photothermal Destruction of Multidrug-Resistant Bacteria. Chem Eur J. 2013; 19:2839–2847. [PubMed: 23296491]
38. Fales AM, Yuan H, Vo-Dinh T. Silica-Coated Gold Nanostars for Combined Surface-Enhanced Raman Scattering (SERS) Detection and Singlet-Oxygen Generation: A Potential Nanoplatform for Theranostics. Langmuir. 2011; 27:12186–12190. [PubMed: 21859159]
39. Harmsen S, Huang R, Wall MA, Karabeber H, Samii JM, Spaliviero M, White JR, Monette S, O'Connor R, Pitter KL, et al. Surface-enhanced Resonance Raman Scattering Nanostars for High-precision Cancer Imaging. Sci Transl Med. 2015; 7:271ra7.
40. Wang M, Cao X, Lu W, Tao L, Zhao H, Wang Y, Guo M, Dong J, Qian W. Surface-enhanced Raman Spectroscopic Detection and Differentiation of Lung Cancer Cell Lines (A549, H1229) and Normal Cell Line (AT II) Based on Gold Nanostars Substrates. RSC Adv. 2014; 4:64225–64234.
41. Wei Q, Song HM, Leonov AP, Hale JA, Oh D, Ong QK, Ritchie K, Wei A. Gyromagnetic Imaging: Dynamic Optical Contrast Using Gold Nanostars With Magnetic Cores. J Am Chem Soc. 2009; 131:9728–9734. [PubMed: 19435348]
42. Huang X, Neretina S, El-Sayed MA. Gold Nanorods: From Synthesis and Properties to Biological and Biomedical Applications. Adv Mater. 2009; 21:4880–4910. [PubMed: 25378252]
43. Link S, El-Sayed MA. Spectral Properties and Relaxation Dynamics of Surface Plasmon Electronic Oscillations in Gold and Silver Nanodots and Nanorods. J Phys Chem B. 1999; 103:8410–8426.
44. Wang H, Brandl DW, Le F, Nordlander P, Halas NJ. Nanorice: A Hybrid Plasmonic Nanostructure. Nano Lett. 2006; 6:827–832. [PubMed: 16608292]
45. Song HM, Wei Q, Ong QK, Wei A. Plasmon-resonant Nanoparticles and Nanostars with Magnetic Cores: Synthesis and Magnetomotive Imaging. ACS Nano. 2010; 4:5163–5173. [PubMed: 20690598]
46. Bhana S, Rai BK, Mishra SR, Wang Y, Huang X. Synthesis and Properties of Near Infrared-Absorbing Magnetic-Optical Nanopins. Nanoscale. 2012; 4:4939–4942. [PubMed: 22806589]
47. Goon IY, Lai LMH, Lim M, Munroe P, Gooding JJ, Amal R. Fabrication and Dispersion of Gold-Shell-Protected Magnetite Nanoparticles: Systematic Control Using Polyethyleneimine. Chem Mater. 2009; 21:673–681.
48. Perdew JP, Burke K, Ernzerhof M. Generalized Gradient Approximation Made Simple. Phys Rev Lett. 1996; 77:3865–3868. [PubMed: 10062328]
49. Kresse G, Joubert D. From Ultrasoft Pseudopotentials to the Projector Augmented-Wave Method. Phys Rev B. 1999; 59:1758–1775.
50. Kresse G, Furthmüller J. Efficient Iterative Schemes for *Ab Initio* Total-Energy Calculations Using a Plane-Wave Basis Set. Phys Rev B. 1996; 54:11169–11186.
51. Draine BT. The Discrete-dipole Approximation and Its Application to Interstellar Graphite Grains. Astrophys J. 1988; 333:848–872.
52. Draine BT, Flatau PJ. Discrete-dipole Approximation for Scattering Calculations. J Opt Soc Am A. 1994; 11:1491–1499.
53. Johnson PB, Christy RW. Optical Constants of The Noble Metals. Phys Rev B. 1972; 6:4370–4379.
54. Goossens V, Wielant J, Van Gils S, Finsy R, Terryn H. Optical Properties of Thin Iron Oxide Films On Steel. Surf Interface Anal. 2006; 38:489–493.
55. Kolhatkar AG, Jamison AC, Litvinov D, Willson RC, Lee TR. Tuning the Magnetic Properties of Nanoparticles. Int J Mol Sci. 2013; 14:15977–16009. [PubMed: 23912237]
56. Oldenburg SJ, Averitt RD, Westcott SL, Halas NJ. Nanoengineering of Optical Resonances. Chem Phys Lett. 1998; 288:243.
57. Nikoobakht B, El-Sayed MA. Preparation and Growth Mechanism of Gold Nanorods (Nrs) Using Seed-Mediated Growth Method. Chem Mater. 2003; 15:1957–1961.

58. Sau TK, Murphy CJ. Room Temperature, High-Yield Synthesis of Multiple Shapes of Gold Nanoparticles in Aqueous Solution. J Am Chem Soc. 2004; 126:8648–8649. [PubMed: 15250706]
59. Orendorff CJ, Murphy CJ. Quantitation of Metal Content in The Silver-Assisted Growth of Gold Nanorods. J Phys Chem B. 2006; 110:3990–3994. [PubMed: 16509687]
60. Sanchez-Gaytan BL, Park SJ. Spiky Gold Nanoshells. Langmuir. 2010; 26(24):19170–19174. [PubMed: 21090617]
61. Sanchez-Gaytan BL, Swanglap P, Lamkin TJ, Hickey RJ, Fakhraai Z, Link S, Park SJ. Spiky Gold Nanoshells: Synthesis and Enhanced Scattering Properties. J Phys Chem C. 2012; 116:10318–10324.
62. Liu M, Guyot-Sionnest P. Mechanism of Silver(I)-assisted Growth of Gold Nanorods And Bipyramids. J Phys Chem B. 2005; 109:22192–22200. [PubMed: 16853888]
63. Sanchez CG, Del Popolo MJ, Leiva EPM. An Embedded Atom Approach to Underpotential Deposition Phenomena. Surf Sci. 1999; 421:59–72.
64. Rojas MI, Sanchez CG, Del Popolo MJ, Leiva EPM. Erratum to: “An embedded atom approach to underpotential deposition phenomena”. Surf Sci. 2000; 453:225–228.
65. Nealon GL, Donnio B, Greget R, Kappler JP, Terazzi E, Gallani JL. Magnetism in Gold Nanoparticles. Nanoscale. 2012; 4:5244–5258. [PubMed: 22814797]
66. Bhana S, Liu G, Wang L, Starring H, Mishra SR, Liu G, Huang X. Near infrared-Absorbing Gold Nanopopcorns with Iron Oxide Cluster Core For Magnetically Amplified Photothermal And Photodynamic Cancer Therapy. ACS Appl Mater Interfaces. 2015; 7:11637–11647. [PubMed: 25965727]
67. Tamer U, Gündoğdu Y, Boyac IH, Pekmez K. Synthesis of Magnetic Core–Shell Fe_3O_4–Au Nanoparticle for Biomolecule Immobilization and Detection. J Nanopart Res. 2010; 12:1187–1196.
68. Pavan Kumar GV, Rangarajan N, Sonia B, Deepika P, Rohman N, Narayana C. Metal-coated Magnetic Nanoparticles For Surface Enhanced Raman Scattering Studies. Bull Mater Sci. 2011; 34:207–216.
69. Carpenter EE, Sangregorio C, O'Connor CJ. Effects of Shell Thickness on Blocking Temperature of Nanocomposites of Metal Particles with Gold Shells. IEEE Trans Magn. 1999; 35:3496–3498.
70. Cho SJ, Kauzlarich SM, Olamit J, Liu K, Grandjean F, Rebbouh L, Long GJ. Characterization and Magnetic Properties of Core/Shell Structured Fe/Au Nanoparticles. J Appl Phys. 2004; 95:6804–6806.
71. Cho SJ, Idrobo JC, Olamit J, Liu K, Browning ND, Kauzlarich SM. Growth Mechanisms and Oxidation Resistance of Gold-Coated Iron Nanoparticles. Chem Mater. 2005; 17:3181–3186.
72. Mandal M, Kundu S, Ghosh SK, Panigrahi S, Sau TK, Yusuf SM, Pal T. Magnetite Nanoparticles with Tunable Gold or Silver Shell. J Colloid Interf Sci. 2005; 286:187–194.
73. Pal S, Morales M, Mukherjee P, Srikanth H. Synthesis and Magnetic Properties of Gold Coated Iron Oxide Nanoparticles. J Appl Phys. 2009; 105:07B504/1–3.
74. Salgueiriño-Maceira V, Correa-Duarte MA, Farle M, López-Quintela A, Sieradzki K, Diaz R. Bifunctional Gold-Coated Magnetic Silica Spheres. Chem Mater. 2006; 18:2701–2706.
75. Hauser JJ. Magnetic Proximity Effect. Phys Rev. 1969; 187:580–586.
76. Crespo P, Litrán R, Rojas TC, Multigner M, de la Fuente JM, Sánchez-López JC, García MA, Hernando A, Penadés S, Fernández A. Permanent Magnetism, Magnetic Anisotropy, and Hysteresis of Thiol-Capped Gold Nanoparticles. Phys Rev Lett. 2004; 93:087204/1–4. [PubMed: 15447222]
77. Nikoobakht B, El-Sayed MA. Evidence for Bilayer Assembly of Cationic Surfactants on the Surface of Gold Nanorods. Langmuir. 2001; 17:6368–6374.
78. Gao J, Bender CM, Murphy CJ. Dependence of the Gold Nanorod Aspect Ratio on the Nature of The Directing Surfactant in Aqueous Solution. Langmuir. 2003; 19:9065–9070.
79. Grzelczak M, Pérez-Juste J, Mulvaney P, Liz-Marzán LM. Shape Control in Gold Nanoparticle Synthesis. Chem Soc Rev. 2008; 37:1783–1791. [PubMed: 18762828]

80. Chaffin E, Bhana S, Huang X, Wang Y. Impact of Core Dielectric Properties on The Localized Surface Plasmonic Spectra of Gold-Coated Magnetic Core Shell Nanoparticles. J Phys Chem B. 2014:14076–14084. [PubMed: 25010347]

81. Hao F, Nehl CL, Hafner JH, Nordlander P. Plasmon Resonances of a Gold Nanostar. Nano Lett. 2007; 7:729–732. [PubMed: 17279802]

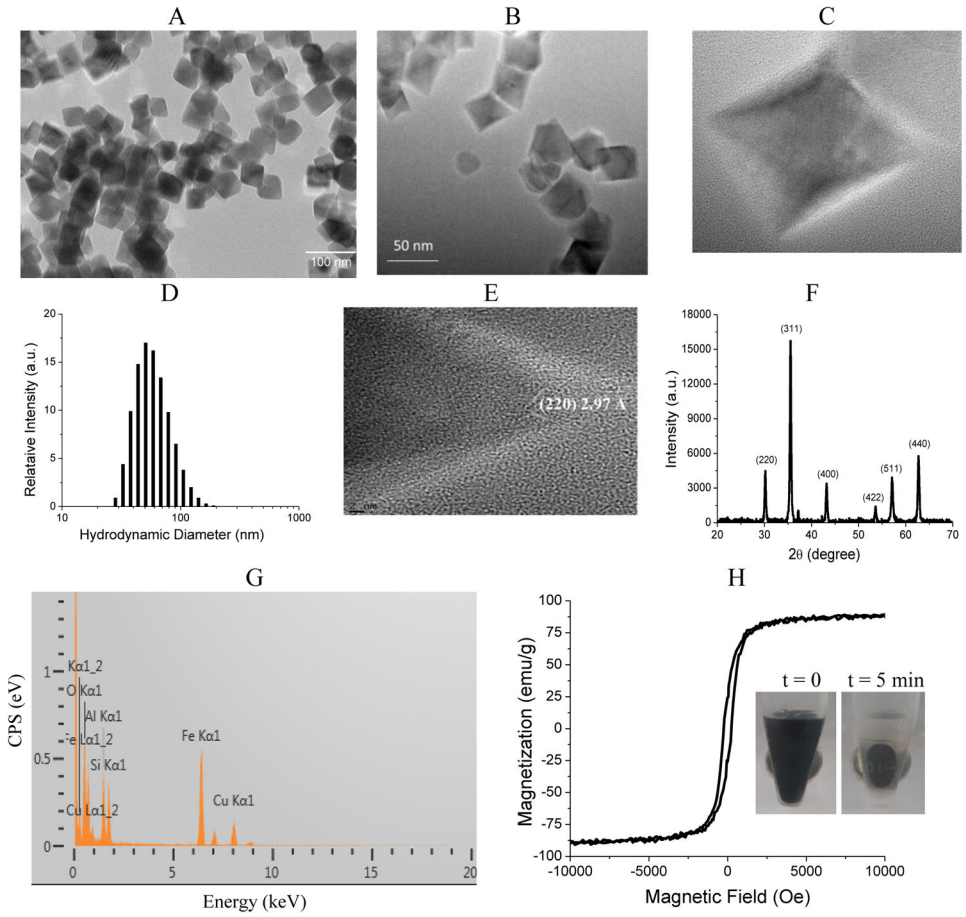

Figure 1.

Structural and magnetic characterizations of IO NPs. (A, B&C) TEM images, (D) DLS plot, (E) HRTEM image, (F) Powder XRD pattern, (G) EDS spectrum, and (H) magnetization as a function of applied field at room temperature. Inset in (H): Optical images of IO NPs with a permanent on at t = 0 and t = 5 min. Image in (A) was taken on a JEM-1200 TEM microscope. Images in (B), (C) and (E) were taken on a FEI Titan HRTEM.

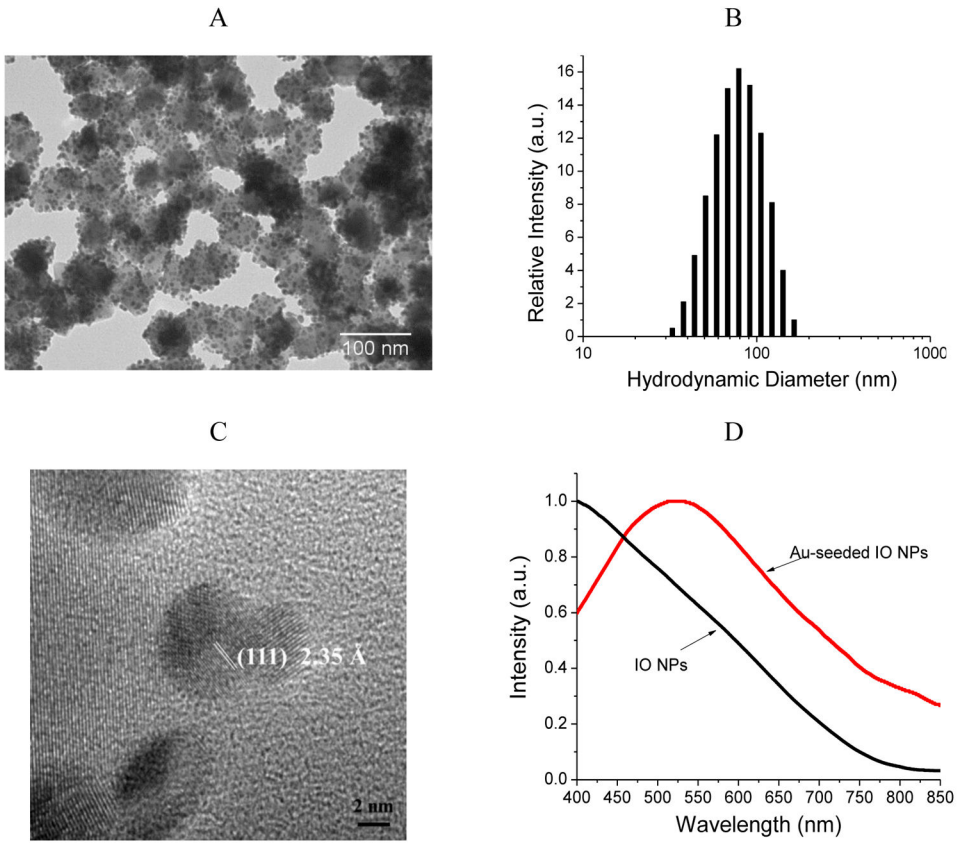

Figure 2.

Structural and optical characterizations of Au-seeded IO NPs. (A) TEM image, (B) DLS plot, (C) absorption spectra, and (D) HRTEM image.

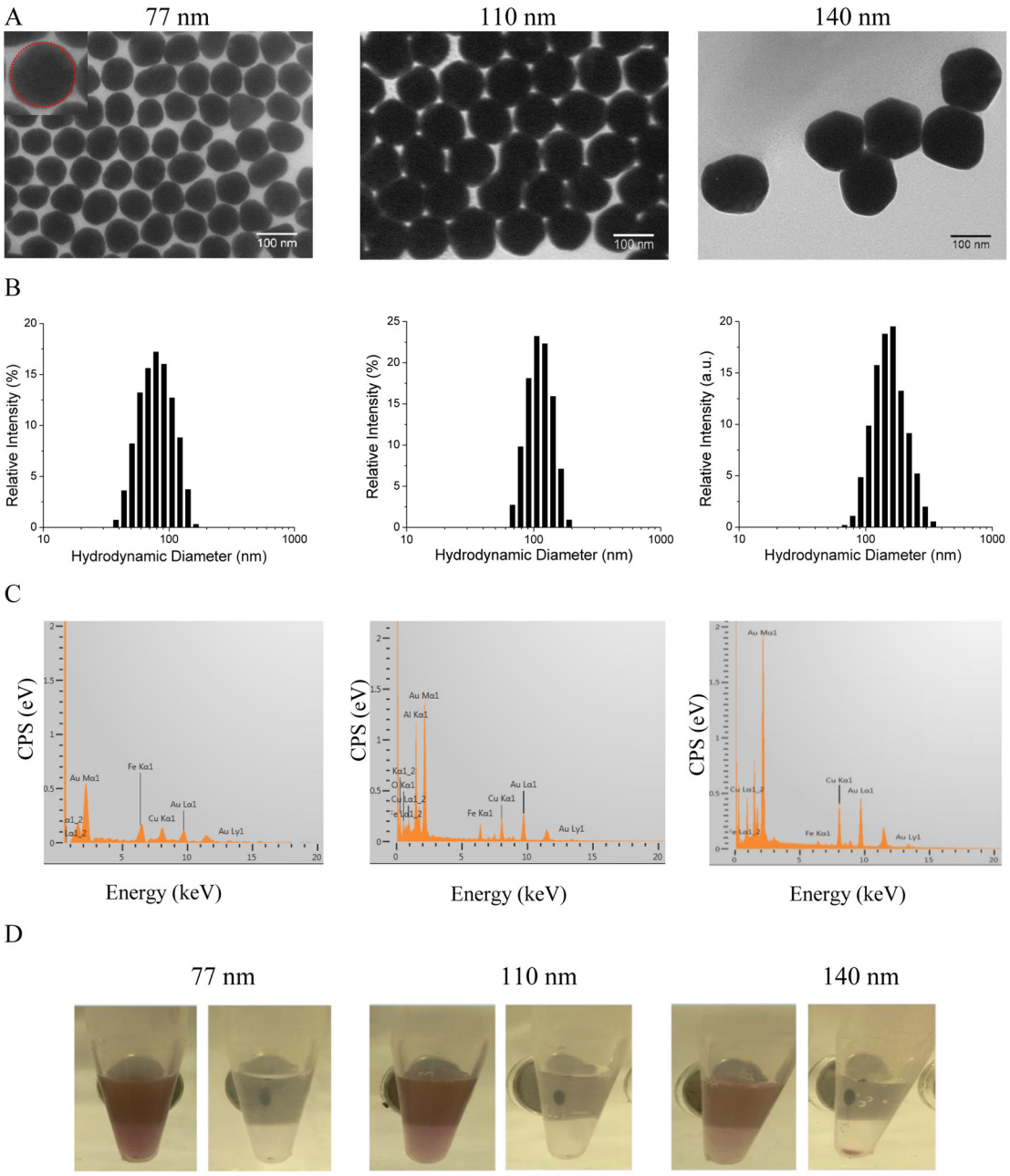

Figure 3.

Characterizations of IO-Au core-shell NSPs of different sizes. (A) TEM images of 77 nm (left), 110 nm (middle), and 140 nm (right) IO-Au core-shell NSPs. Each size was determined by averaging the diameter from ~100 NPs in a spherical geometry (see inset illustration) from the TEM images. (B) DLS plots. (C) EDS spectra. (D) Optical images of IO-Au NSP solutions before and after magnetic separation.

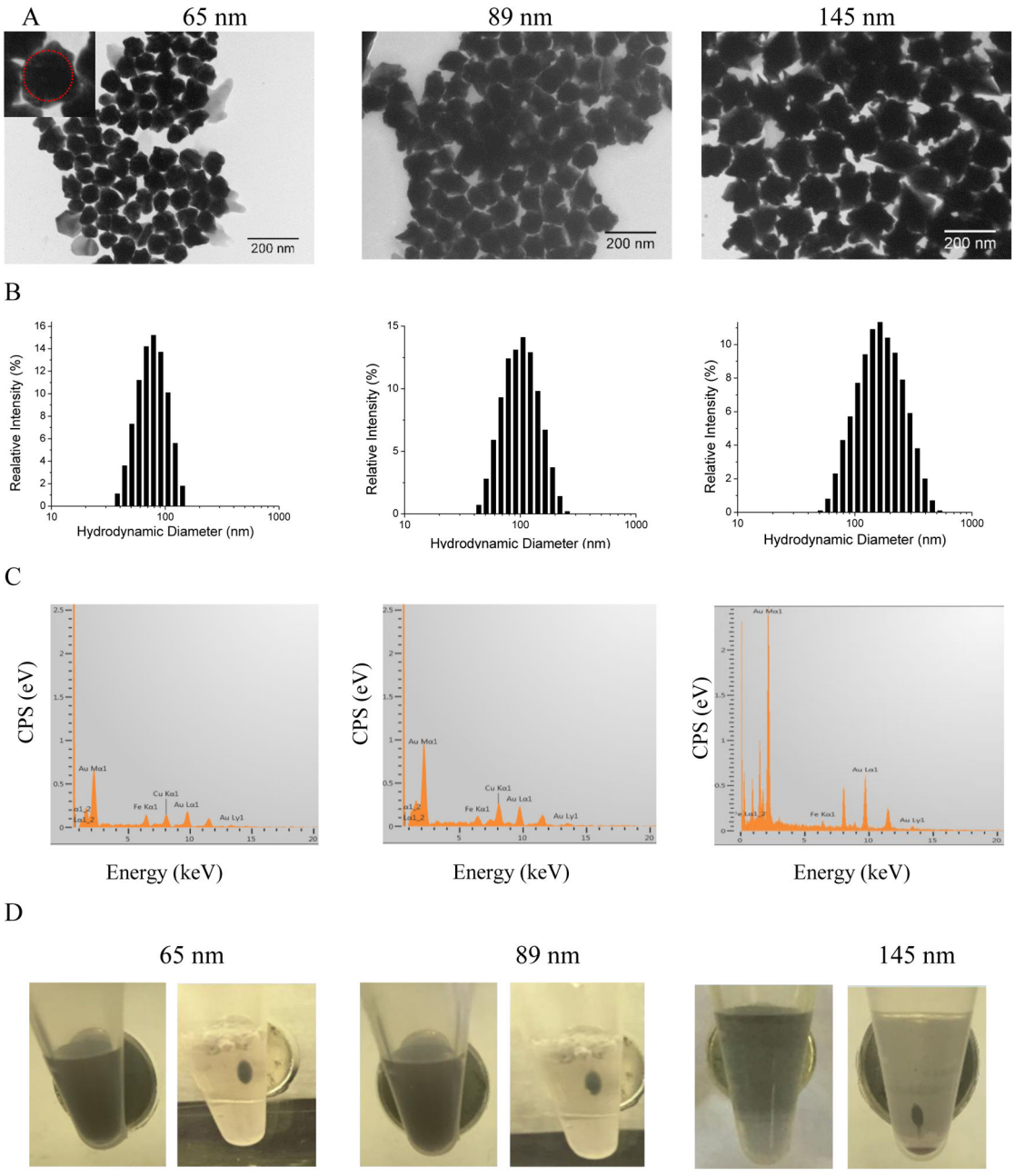

Figure 4.

Characterizations of IO-Au core-shell NPCs of different sizes. (A) TEM images of 65 nm (left), 89 nm (middle) and 145 nm (right) IO-Au core-shell NSPs. Each size was determined by averaging the diameter from ~100 NPs in a spherical geometry (see inset illustration) from the TEM images. (B) DLS plots. (C) EDS spectra. (D) Optical images of IO-Au NPCs before and after magnetic separation.

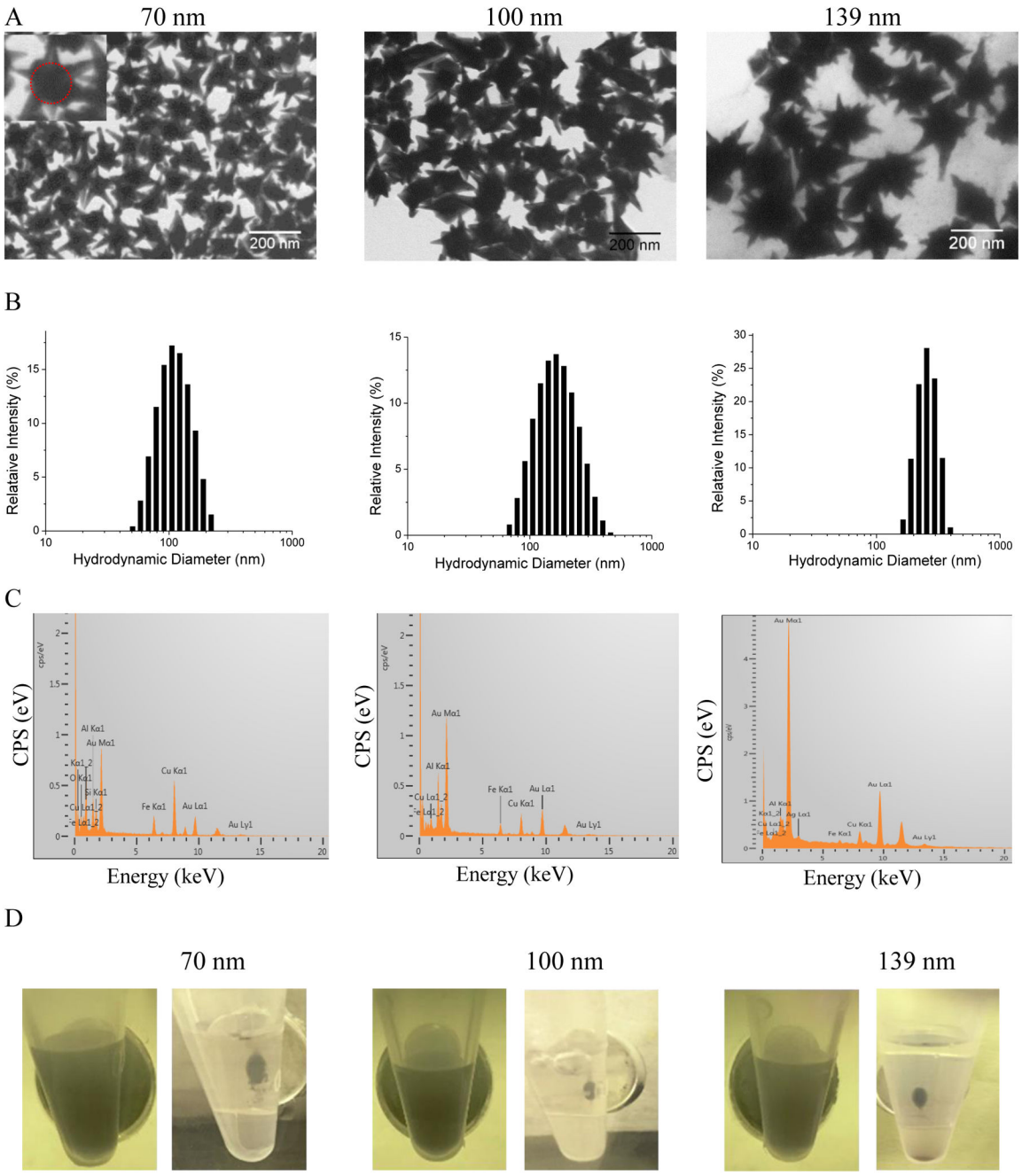

Figure 5.

Characterizations of IO-Au core-shell NSTs of different sizes. (A) TEM images of 70 nm (left), 100 nm (middle) and 139 nm (right) IO-Au core-shell NSPs. Each size was determined by averaging the diameter from ~100 NPs in a spherical geometry (see inset illustration) from the TEM images. (B) DLS plots. (C) EDS spectra. (D) Optical images of IO-Au NSTs before and after magnetic separation.

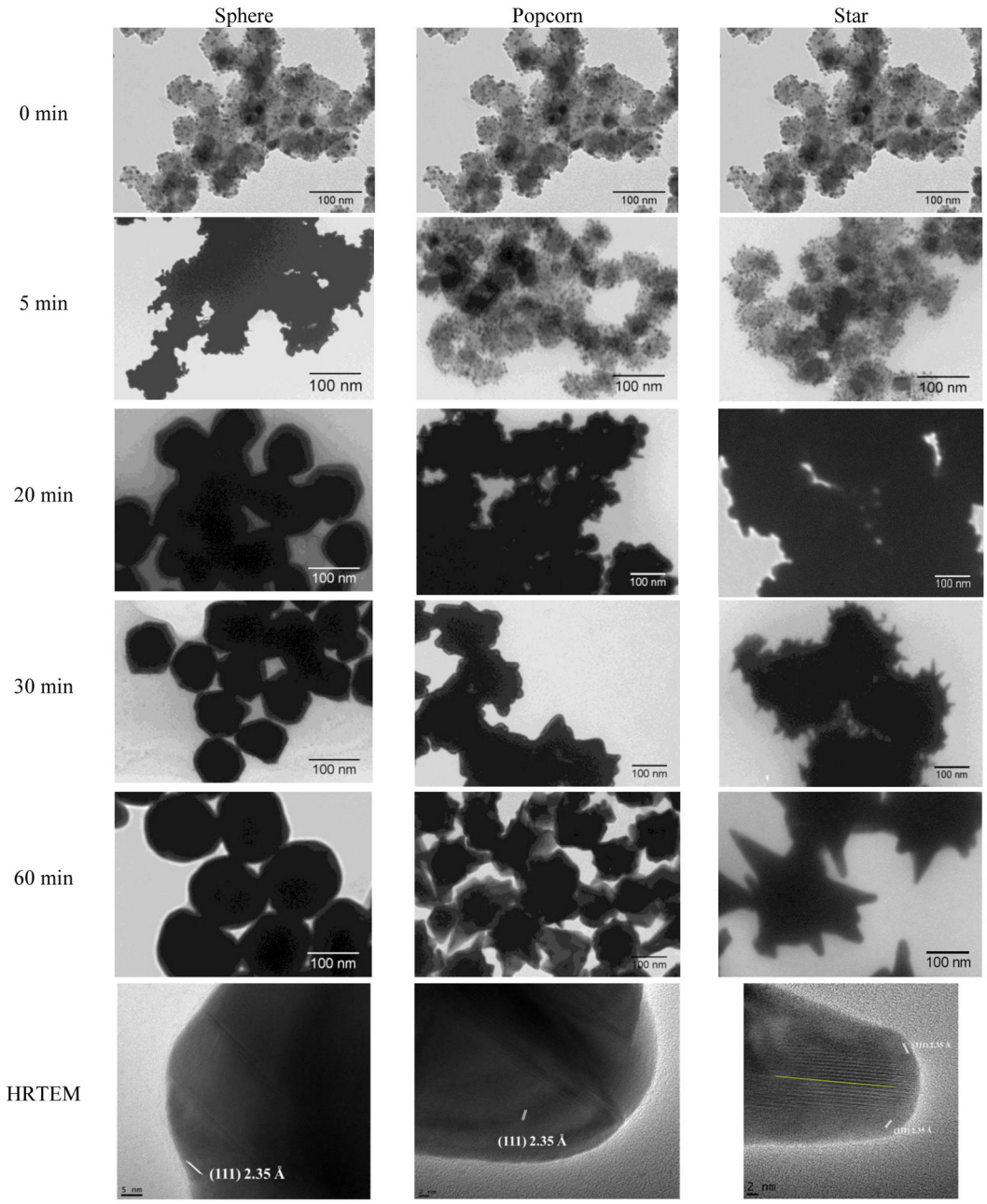

Figure 6.

Monitoring the growth process of IO-Au core-shell NPs in different shapes by TEM imaging at different time after the injection of Au-seeded IO NPs into the growth solution. The yellow line in the HRTEM image for the star shows twinned defect. The same image in the top row is used for all shapes to indicate that the same sample of Au-seeded IO NPs was used during the synthesis.

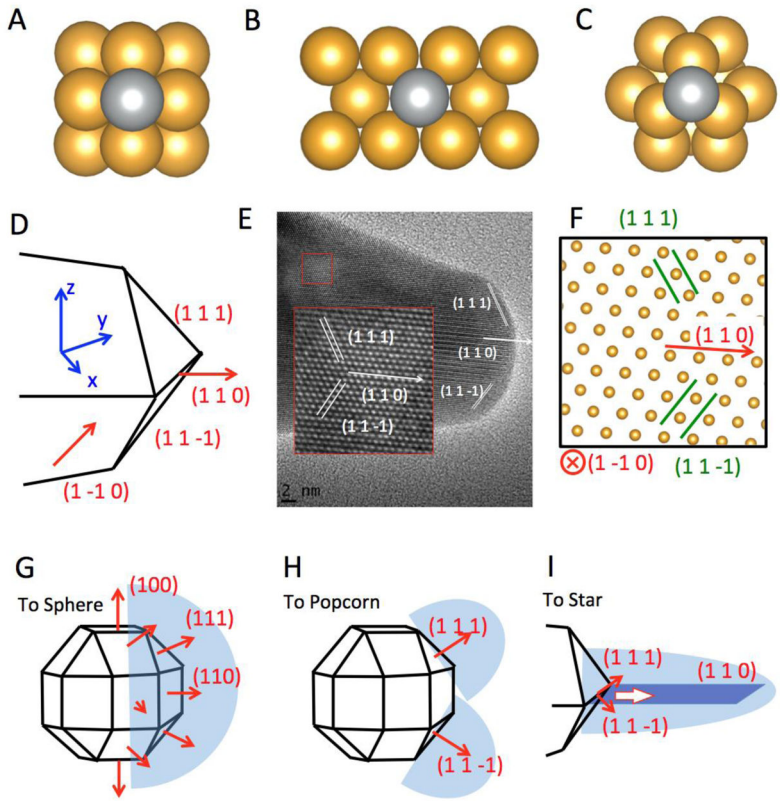

Figure 7.

Computational studies on growth mechanism. (A) The adsorption of Ag on Au (100) surface. (B) The adsorption of Ag on Au (110) surface. (C) The adsorption of Ag on Au (111) surface. (D) Schematic of the proposed geometry of the tip of the nanostar. (E) HRTEM image of a tip of the nanostar. The insert shows an enlarged view of the lattice, where the position of each atom is visible. (F) The positions of atoms according to the proposed model in (D), which is viewed from the [1 −1 0] direction. (G) The growth mechanism of Au nanosphere. (H) The growth mechanism of Au nanopopcorn. (I) The growth mechanism of a tip of Au nanostar. The twin boundary, which corresponds to the yellow line in the lower right of Figure 6, is marked in dark blue color.

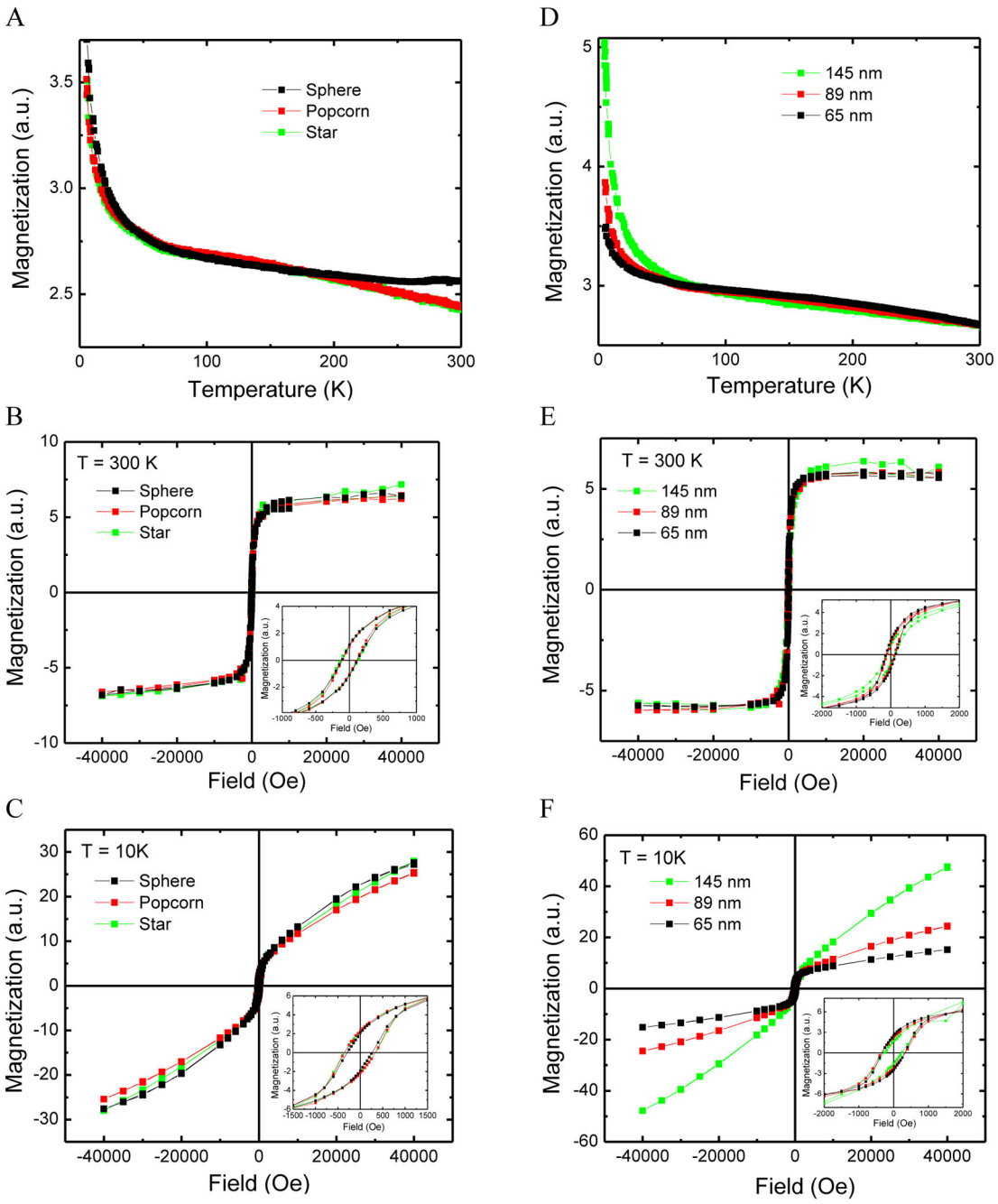

Figure 8.

Comparison of the magnetic properties of IO-Au core-shell NPs by shape and size. (A) Magnetization as a function of temperature for IO-Au NSPs, NPCs and NSTs. Magnetization as a function of applied field for NSPs, NPCs, and NSTs around 100 nm at 300 K (B) and 10 K (C). (D) Magnetization as a function of temperature for IO-Au NPCs of three different sizes. Magnetization as a function of applied field for IO-Au NPCs of three different sizes at 300 K (E) and 10 K (F). The insets in (B), (C), (E), and (F) show the hysteresis loops under low magnetic field.

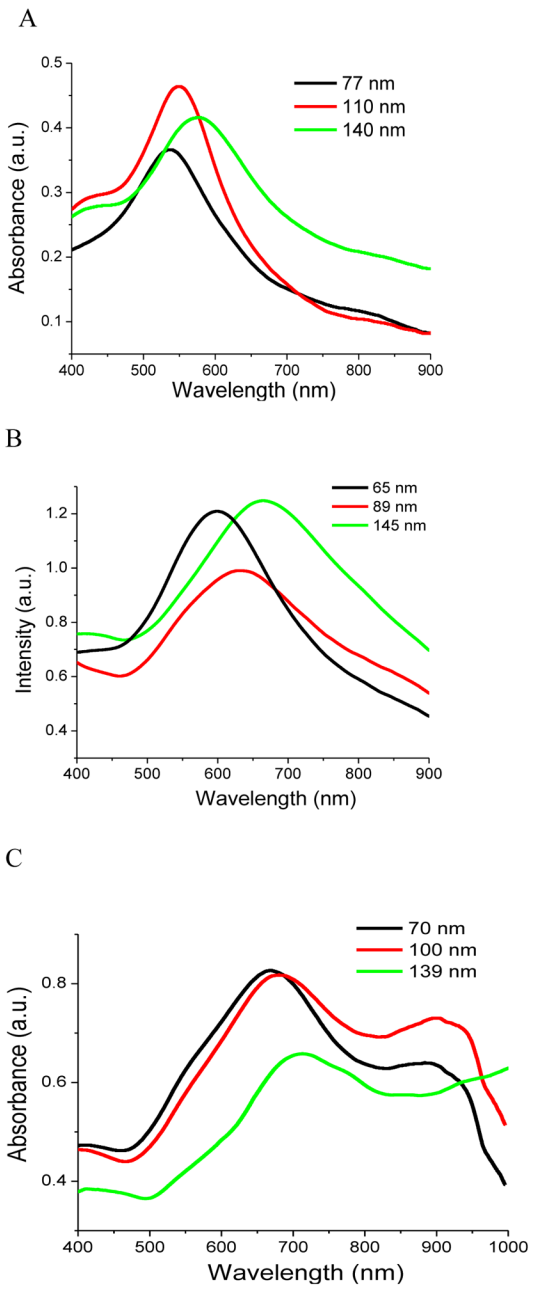

Figure 9.

Absorption spectra of IO-Au core-shell NSPs (A), NPCs (B) and NSTs (C) of different sizes. The sizes labeled in the graphs are the base size of the particles that do not include the protrusions in popcorns and tips in the stars.

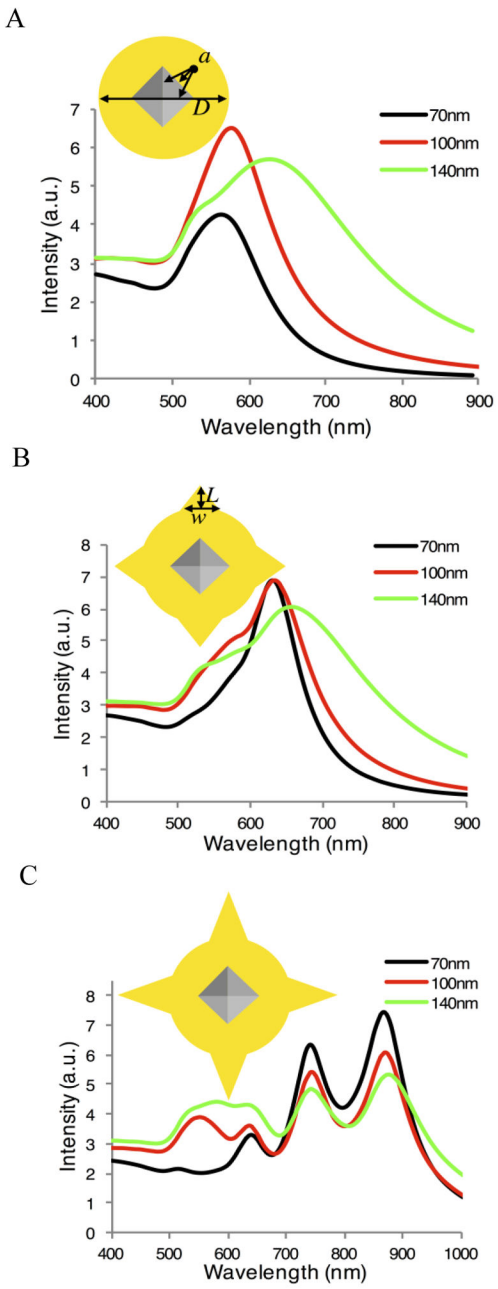

Figure 10.

Calculated extinction spectra for the three sizes (D = 70, 100, and 140 nm) of IO-Au core-shell NPs with octahedral IO cores (edge length a = 35 nm). (A) IO-Au core-shell NSPs (no tips). (B) IO-Au core-shell NPCs modeled by adding six conical tips with L = 20 nm and w = 30 nm. (C) IO-Au core-shell NSTs modeled by adding six conical tips with L = 40 nm and w = 30 nm. The inserts are the 100 nm particle models shown to scale.

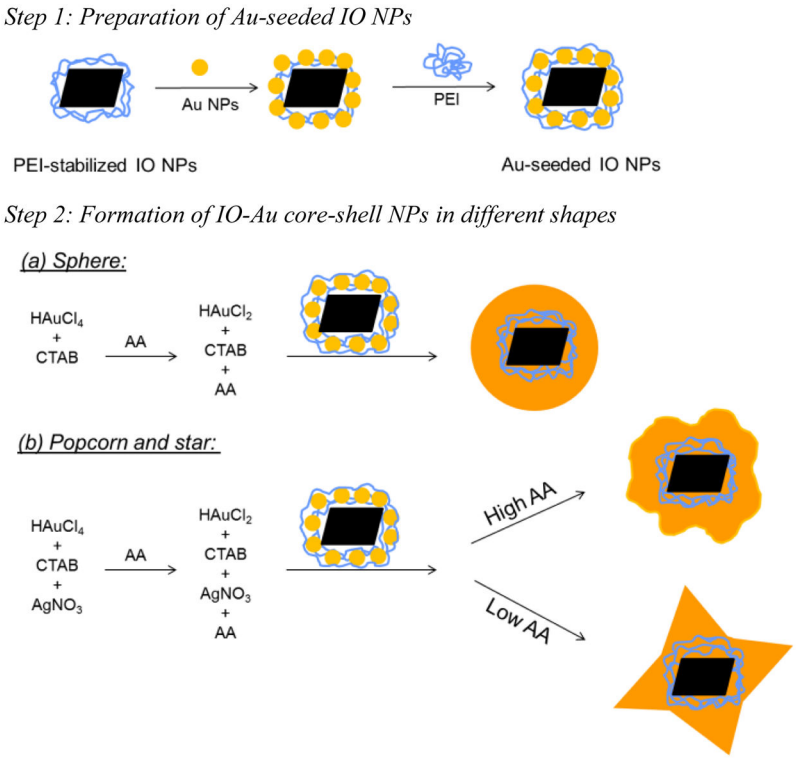

Scheme 1.

Synthesis of IO-Au core-shell NPs in different shapes. Au-seeded IO NPs were prepared by electrostatic adsorption of small Au NPs onto PEI-stabilized IO NPs, followed by further stabilization with PEI. The growth of IO-Au core-shell NPs were initiated by injecting Au-seeded IO NPs into a growth solution containing chloroauric acid ($HAuCl_4$), silver nitrate ($AgNO_3$), cetyltrimethylammonium bromide (CTAB) and ascorbic acid (AA).

Table 1

Characterizations of the size distribution of IO-Au core-shell NPs of different shapes. D_{av}: the average diameter (~ 100 NPs) of the IO-Au spherical base core measured by TEM (see Figure 3(A)–5(A) the left panel inset for illustration). σ (%): standard deviation. D_{hydro}: the average hydrodynamic diameter measured by DLS. L_{tip}: the length of the protrusions on the IO-Au spherical core. $W_{1/2tip}$: the half length of the protrusions.

	TEM size analysis				**DLS size analysis**		**Absorption property**
	D_{av} (nm)	**σ (%)**	**$L_{tip\ (nm)}$**	**$W_{1/2tip}$ (nm)**	**D_{hydro} (nm)**	**σ (%)**	**LSPR (nm)**
Spheres	77	5	N/A	N/A	84	11	538
	110	8	N/A	N/A	122	14	550
	140	8	N/A	N/A	155	19	575
Popcorn	65	5	5–35	10–40	80	16	600
	89	9	5–55	10–50	110	18	633
	145	17	15–65	15–62	170	21	665
Stars	70	7	10–75	5–25	105	38	550, 660, 895
	100	10	15–90	10–30	160	24	550, 684, 920
	139	8	20 – 145	20–67	250	30	550, 715, > 950